International Journal of Control, Automation and Systems 20(2) (2022) 678-690
http://dx.doi.org/10.1007/s12555-020-0694-0
ISSN:1598-6446 eISSN:2005-4092
http://www.springer.com/12555

Adaptive Back-stepping Neural Control for an Embedded and Tiltable V-tail Morphing Aircraft

Fuxiang Qiao , Jingping Shi* , Xiaobo Qu , and Yongxi Lyu

Abstract: This paper presents an adaptive back-stepping neural control (ABNC) method for the coupled nonlinear model of a novel type of embedded surface morphing aircraft. Based on a large number of aerodynamic data for different V-tail configurations, the longitudinal and lateral aerodynamic characteristics of the aircraft are analyzed, and a nonlinear model with six degrees-of-freedom is established. To avoid the problem of "differential explosion," the controller is designed using the traditional back-stepping control (TBC) method with a first-order filter. Radial basis function neural networks are introduced to estimate the uncertainty and external disturbance of the model, and a controller based on the ABNC method is designed. The stability of the proposed ABNC controller is proved using Lyapunov theory, and it is shown that the tracking error of the closed-loop system converges uniformly within specified bounds. Simulation results show that the ABNC controller works well, with better tracking performance and robustness than the TBC controller.

Keywords: Adaptive control, back-stepping control, morphing aircraft, neural networks, radial basis function.

NOMENCLATURE

α, β	Angle of attack, sideslip angle
χ	Yaw angle in trace coordinate frame (ground track angle)
γ	Pitch angle in trace coordinate frame (climb angle)
μ	Roll angle in trace coordinate frame
C_*	Dimensionless aerodynamic coefficient of *
D, Y, L	Aerodynamic forces in the wind-fixed reference frame
M_l, M_m, M_n	Aerodynamic rolling, pitching, and yawing moments
p, q, r	Roll, pitch, and yaw rates around the body-fixed reference frame
Q	Dynamic pressure
T	Thrust force
V	Velocity of aircraft
x_E, y_E, z_E	Position of the aircraft in the inertial reference frame (earth)

1. INTRODUCTION

The study of morphing aircraft has received considerable interest due to the superior flight performance of such vehicles, which is achieved by altering the aerodynamic configuration and adapting to different flight environments [1–3]. The force and moment characteristics of a morphing aircraft can change significantly through the variation of its aerodynamic configuration, enabling dramatic enhancements in flight performance and combat effectiveness [4–8]. Various types of morphing aircraft have been proposed for different purposes. To solve the problem of the poor lateral stability of tailless blended wing/body aircraft, this paper presents a new type of embedded surface morphing aircraft with an adjustable V-tail.

In previous research, most control schemes focus on the control of sweep-back wings, similar to Firebee [9] or MFX-2 [10]. Wu *et al*. [11] proposed an adaptive neural controller for the longitudinal dynamics of a sweep-back-wing morphing aircraft based on a high-order integral chained differentiator. A composite switching neural prescribed-performance control scheme has been presented [12], and a modified adaptive neural dynamic surface control approach has been developed for the longi-

Manuscript received September 20, 2020; revised March 3, 2021; accepted April 28, 2021. Recommended by Associate Editor Aldo Jonathan Munoz-Vazquez under the direction of Editor Chan Gook Park. This research was supported by the National Natural Science Foundation of China (Grant No. 61573286), Aeronautical Science Foundation of China (Grant No. 20180753006), Fundamental Research Funds for the Central Universities (grant No. 3102019ZDHKY07), Natural Science Foundation of Shaanxi Province (Grant No. 2020JQ-218), and Shaanxi Province Key Laboratory of Flight Control and Simulation Technology.

Fuxiang Qiao, Jingping Shi, Xiaobo Qu, and Yongxi Lyu are with the School of Automation, Northwestern Polytechnical University, Xi'an 710129, China (e-mails: {fuxiang_qiao, yongxi_lyu}@mail.nwpu.edu.cn, {shijingping, xiaobo}@nwpu.edu.cn). Jingping Shi, Xiaobo Qu, and Yongxi Lyu are also with the Shaanxi Province Key Laboratory of Flight Control and Simulation Technology, Xi'an 710129, China.
* Corresponding author.

©ICROS, KIEE and Springer 2022

tudinal dynamics with unknown parameters and input–output constraints [13]. Wang *et al*. [14] investigated the control problem of a similar model with variable-sweep wings based on switched nonlinear systems and adaptive dynamic programming, modeling the longitudinal altitude motion as a switched nonlinear system in lower triangular form. Yan *et al*. [15] proposed a longitudinal dynamic model of a variable-sweep-wing morphing aircraft based on the Firebee unmanned aerial vehicle (UAV), and designed a classic proportional–integral–derivative (PID) controller with different gains. They then designed an adaptive super-twisting algorithm sliding mode controller [16]. A multi-body dynamic model of an asymmetric variable-sweep-wing morphing UAV based on Kane's method was reported in [17]. The asymmetric wing-sweep morphing was used as the roll controller instead of the aileron in the flight control, and trajectory tracking control via a constrained back-stepping method was presented.

Several scholars have studied other types of morphing aircraft and corresponding control methods. Grant *et al*. [18] designed a multiple-joint variable-sweep morphing aircraft, inspired by highly agile birds. The left and right wings, as well as the inboard and outboard sections of this aircraft, can vary independently. The variations admitted by a multi-joint mechanism were studied using computational vortex lattice methods. Grant *et al*. then advanced their work by investigating the longitudinal dynamics of this aircraft from the perspective of flight dynamics, and proposed a time-varying characteristic equation for the influence of different morphing trajectories [19]. In [20], a longitudinal linear parameter varying model of a folding-wing morphing aircraft with a varying wing shape was investigated, and the longitudinal dynamic responses of the aircraft during wing folding were simulated under a quasi-steady aerodynamic assumption. A pair of linear controllers based on the self-scheduled gain H_∞ robust control system was designed to guarantee stability for the wing-shape-varying process [21]. Later, a hypersonic morphing aircraft with retracted winglets based on X-24B was researched and a novel learning method for the control law of mode switching based on a type-2 Takagi–Sugeno–Kang fuzzy neural network was proposed [22]. In [23], a tailless telescopic-wing morphing aircraft was studied, and the dynamic response of asymmetric wing telescoping was simulated and analyzed. Finally, a sliding mode flight controller was proposed to enhance the lateral maneuverability using additional symmetric wing telescoping. Inspired by a pigeon's wing structure, Hui *et al*. [24] designed a bio-inspired morphing discrete wing configuration. The aerodynamic performance of wing configurations with different morphing states were also investigated in detail. Xu *et al*. [25] extended this work by addressing the autonomous shape optimization problem of intelligent morphing aircraft according to mission requirements and flight status based on deep neural networks and reinforcement learning techniques.

Although the designs and control schemes of morphing aircraft have made significant progress in recent years, several phenomena and difficulties need to be addressed: 1) Most studies take the sweep-back-wing morphing aircraft as the control object. 2) The decoupled longitudinal model is mainly used for controller design and performance analysis. In essence, the controlled object is a single input–single output model, which makes it difficult to reflect the complexity of morphing aircraft and the actual performance of the controller. 3) Most previous studies have only considered the control of the longitudinal system, rather than considering the longitudinal and lateral dynamics as a whole system.

The motivation of this paper is to present an adaptive back-stepping neural control (ABNC) method for the coupled nonlinear model of a novel type of embedded surface morphing aircraft. The main contributions of this paper are summarized as follows:

1) A novel morphing aircraft is explicitly designed to adapt to different flight environments and missions. Based on a large number of aerodynamic data from different V-tail configurations, the longitudinal and lateral aerodynamic characteristics of the aircraft are analyzed, and a nonlinear model with six degrees-of-freedom is established.

2) A first-order filter is incorporated into the traditional back-stepping control (TBC) design to avoid the problem of "differential explosion." Moreover, radial basis function (RBF) neural networks are introduced to estimate the uncertainty and external disturbance of the model, and a controller based on the ABNC method is designed. Unlike studies that focus solely on a linearized model with separate longitudinal dynamics, both of the controllers presented in this paper are designed for the longitudinal and lateral dynamics of the system.

3) A Lyapunov synthesis based on stability analysis is used to prove the stability of the closed-loop system.

The remainder of this paper is organized as follows: Section 2 introduces the morphing aircraft model and aerodynamic parameters. In Section 3, the traditional back-stepping controller is designed. On the basis of Section 3, Section 4 presents an adaptive back-stepping neural controller and the associated stability analysis. Simulation results are presented and discussed in Section 5. Finally, Section 6 summarizes the conclusions from this study and gives some ideas for future work.

2. AIRCRAFT AERODYNAMICS AND MODEL

2.1. XQ-8A specification

A novel type of embedded surface morphing aircraft, named XQ-8A, has been devised by a research group at the Northwestern Polytechnical University, Xi'an. The

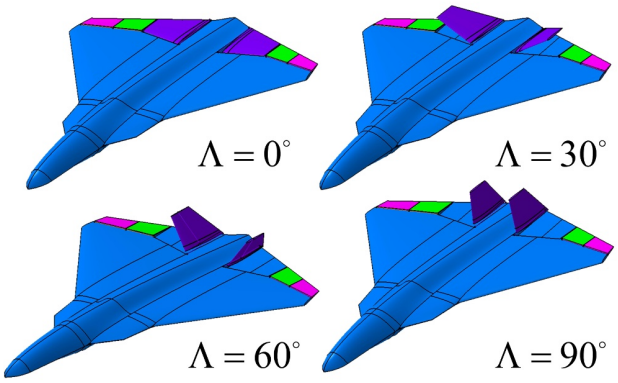

Fig. 1. Different configurations of XQ-8A.

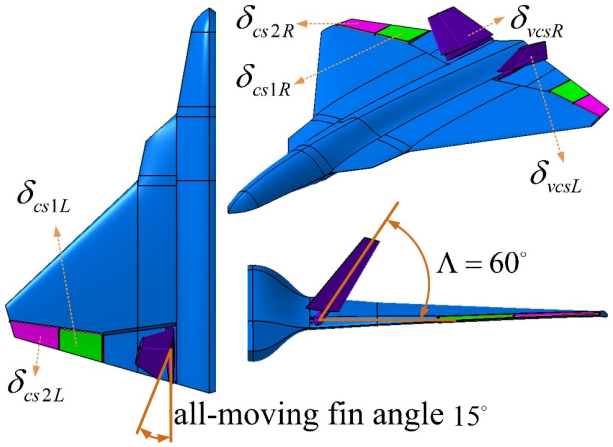

Fig. 2. Definition of flight control surfaces and angles.

XQ-8A, which is shown in Fig. 1, has four empennage surfaces and a pair of variable flight control surfaces, which can form a V-tail or be embedded in the fuselage. There are twin all-moving fins, as shown in Fig. 2. When the angle of the V-tail is zero ($\Lambda = 0°$), the control surfaces are embedded in the fuselage and the aircraft has a flying-wing configuration. Due to the mechanical dead zone, when the angle of the V-tail is less than 15 degrees ($\Lambda < 15°$), the all-moving fins cannot deflect. Thus, only when the angle of the V-tail is greater than or equal to 15 degrees ($\Lambda \geq 15°$) do the all-moving fins actually work, operating as a rudder. The other two pairs of empennage surfaces in Fig. 2 can be divided into an inner control surface (CS1) and an outer control surface (CS2) according to their positions. The takeoff weight of this aircraft is 28 kg and the cruise speed is designed to be 150 km/s at an altitude of 1000 m. The other key parameters of the XQ-8A are listed in Table 1.

The novel morphing aircraft is designed to adapt to different flight environments and missions. When the angle of the V-tail is small, the aircraft has a blended wing–body aerodynamic configuration. This has many advantages, such as reducing the radar cross section and improving the aircraft's lift-to-drag ratio, which results in an extended flight range. However, this aerodynamic configuration reduces the directional stability and maneuverability of the aircraft. When the V-tail angle is increased, the maneuverability and lateral stability of the aircraft will increase, but the stealth performance and flight range of the aircraft will decrease. Therefore, this morphing aircraft needs to adapt to different flight environments and missions by altering the V-tail configuration.

Table 1. Main parameters of XQ-8A.

Parameter	Notation	Value
Aircraft mass	m	28 kg
Wingspan	b	1.512 m
Wing area	S	1.226 m^2
Mean aerodynamic chord	c_A	1.031 m
Distance from nose to center of gravity of the fuselage	x_{cg}	1.04395 m
Moment of inertia	I_x	1.246 kg·m^2
	I_y	3.777 kg·m^2
	I_z	5.009 kg·m^2
Product of inertia	I_{xz}	0.1382 kg·m^2
	I_{xy}	0.0 kg·m^2
	I_{yz}	0.0 kg·m^2

For this aircraft, different modes of control surface allocation must be devised according to the different V-tail angle. For instance, the four empennage control surfaces (δ_{cs1R}, δ_{cs1L}, δ_{cs2R}, δ_{cs2L}) can be used as elevons, and the all-moving fins (δ_{vcsR}, δ_{vcsL}) located on the V-tail can be used as a rudder when the angle of the V-tail is greater than 15 degrees ($\Lambda \geq 15°$). Under this control surface allocation mode, the four elevons control the pitching and rolling motion of the aircraft, and the all-moving fins are used for yaw control.

However, the all-moving fins cannot deflect when the angle of the V-tail is less than 15 degrees ($\Lambda < 15°$); therefore, a new control surface allocation scheme is needed for such configurations. The idea of the first scheme is to use four elevons to control the pitching and rolling motion and reduce the sideslip angle. This scheme becomes an underactuated control problem. The other scheme uses CS1 as the elevons to control the pitching and rolling motion, with CS2 used as the drag rudders to control the yaw of the aircraft. Additionally, some control methods determine the deflection of the flight control surfaces using the matrix of steering efficiency.

The range of flight control surfaces CS1 and CS2 (δ_{cs1R}, δ_{cs1L}, δ_{cs2R}, δ_{cs2L}) is limited to $-20° \sim 20°$. The position limit of the all-moving fins (δ_{vcsR}, δ_{vcsL}) is $-15° \sim 15°$ when the angle of the V-tail exceeds 15 degrees ($\Lambda \geq 15°$).

2.2. Aerodynamics analysis

The aerodynamic forces and moments are obtained using computational fluid dynamics, and then transformed into dimensionless aerodynamic coefficients in the body-axis and wind-axis frames. The approximate aerodynamic models are expressed in (1) and (2) and Appendix A.

$$\begin{cases} C_L = C_{Lstatic} + \left(\mathbf{C}_L^{\delta}\right)^{\mathrm{T}} \boldsymbol{\delta} + C_L^q \left(\dfrac{qc_A}{2V}\right), \\ C_D = C_{\mathrm{Dstatic}} + \left(\mathbf{C}_D^{\delta}\right)^{\mathrm{T}} \boldsymbol{\delta}, \\ C_Y = C_{\mathrm{Ystatic}} + !\left(\mathbf{C}_Y^{\delta}\right)^{\mathrm{T}} \boldsymbol{\delta} + C_Y^p \left(\dfrac{pb}{2V}\right) + C_Y^r \left(\dfrac{rb}{2V}\right), \end{cases} \tag{1}$$

$$\begin{cases} C_l = C_{l\mathrm{static}} + \left(\mathbf{C}_l^{\delta}\right)^{\mathrm{T}} \boldsymbol{\delta} + C_l^p \left(\dfrac{pb}{2V}\right) + C_l^r \left(\dfrac{rb}{2V}\right), \\ C_m = C_{\mathrm{mstatic}} + \left(\mathbf{C}_m^{\delta}\right)^{\mathrm{T}} \boldsymbol{\delta} + C_m^q \left(\dfrac{qc_A}{2V}\right), \\ C_n = C_{\mathrm{nstatic}} + \left(\mathbf{C}_n^{\delta}\right)^{\mathrm{T}} \boldsymbol{\delta} + C_n^p \left(\dfrac{pb}{2V}\right) + C_n^p \left(\dfrac{pb}{2V}\right), \end{cases} \tag{2}$$

where the vector $\delta = [\delta_{cs1R}, \delta_{cs1L}, \delta_{cs2R}, \delta_{cs2L}, \delta_{vcsR}, \delta_{vcsL}]^{\mathrm{T}}$ denotes the deflection of the control surfaces, and the vector $\mathbf{C}_*^{\delta} = [C_*^{cs1R}, C_*^{cs1L}, C_*^{cs2R}, C_*^{cs2L}, C_*^{vcSR}, C_*^{vcSL}]^{\mathrm{T}}$ denotes the aerodynamic derivative of $*$ ($* = \{L, D, Y, l, m, n\}$). The detailed aerodynamic coefficients and data are illustrated in the following figures.

2.2.1 Longitudinal aerodynamic data

The longitudinal aerodynamic data ($\beta = 0°$) of the XQ-8A are shown in Fig. 3. The overall lift-to-drag ratio is greater than 10 for all configurations of the V-tail when α is in the range $[2°, 6°]$. The maximum lift-to-drag ratio is about 13.8 when the angle of the V-tail is zero. When $\alpha < 12°$, the influence of the V-tail angle on the coefficients of lift, drag, and pitching moment are small and can be neglected. The derivative of the pitch moment coefficient with respect to the angle of attack is less than zero ($C_m^{\alpha} < 0$), which means the pitch of the aircraft is statically stable. When $\alpha > 12°$, the influence of the V-tail angle on these aerodynamic coefficients is obvious, especially for the pitching motion coefficient.

The geometric positions of CS1R and CS2R (δ_{cs1R}, δ_{cs2R}) are symmetrical about the aircraft's symmetry plane Oxz, so the effects of CS1L and CS2L (δ_{cs1L}, δ_{cs2L}) on the longitudinal aerodynamic force and aerodynamic moment are the same when they deflect independently. The lateral aerodynamic force and aerodynamic moment of the left-side control surfaces (δ_{cs1L}, δ_{cs2L}) have the same amplitude as those of the right side (δ_{cs1R}, δ_{cs2R}), but the polarity is opposite. This rule also applies to the all-moving fins (δ_{vcsR}, δ_{vcsL}). Therefore, only the control coefficients of the right-side control surfaces are discussed in this paper.

2.2.2 Lateral aerodynamic data

The lateral aerodynamic data of the aircraft are shown in Fig. 4. The variation of the aerodynamic coefficients is illustrated at different angles of attack, sideslip angles, and V-tail angles.

In all V-tail configurations, when $|\beta| < 18°$, the variation in the lift coefficient and drag coefficient is quite small, which means the influence of the sideslip angle on the aircraft drag and lift characteristics is not obvious. The increment of the pitching moment coefficient

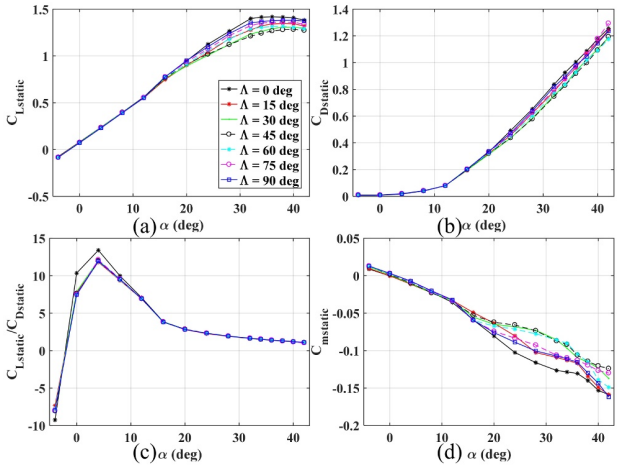

Fig. 3. Longitudinal aerodynamic data.

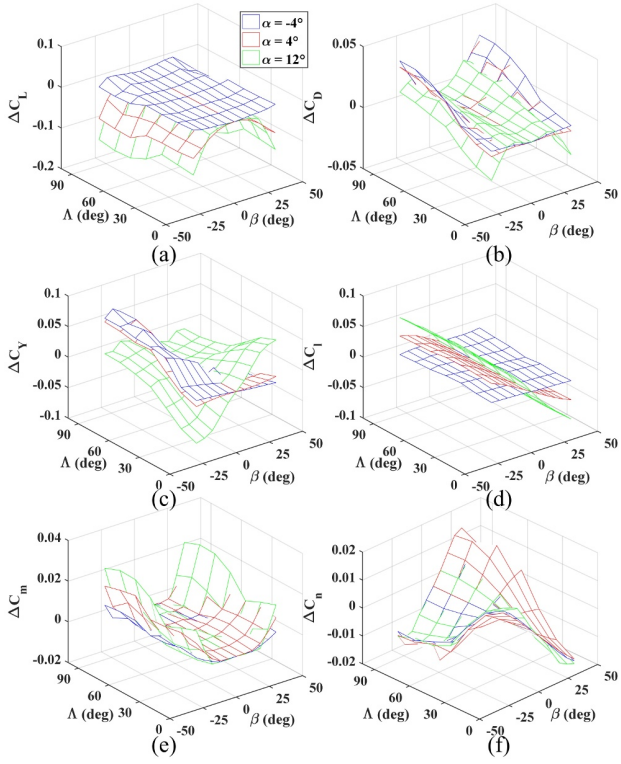

Fig. 4. Lateral aerodynamic data.

ΔC_m caused by the sideslip angle is also insignificant in this case. When the angle of attack is small ($\alpha < 12^\circ$), the V-tail angle changes from zero to 90 degrees, and the variation of the side-force coefficient ΔC_Y caused by the sideslip angle is not obvious, especially when the V-tail angle ranges from 0–30 degrees.

In Fig. 4(d), for all configurations of the V-tail, the derivative of the roll moment coefficient with respect to the sideslip angle is less than zero ($C_l^\beta < 0$), so the rolling of the aircraft is statically stable. Fig. 4(f) shows that the polarity of C_n^β (the derivative of the yaw moment coefficient with respect to the sideslip angle) is related to the V-tail angle. When $\Lambda < 30^\circ$, $C_n^\beta > 0$, so the yaw of the aircraft is statically unstable. When $\Lambda > 45^\circ$, $C_n^\beta < 0$, the yaw of the aircraft becomes statically stable.

2.3. Dynamic model

The relevant nonlinear equations of motion used for the controller design are as follows:

$$\begin{cases} \dot{x}_E = V\cos\gamma\cos\chi, \\ \dot{y}_E = V\cos\gamma\sin\chi, \\ \dot{h} = -\dot{z}_E = V\sin\gamma, \end{cases} \tag{3}$$

$$\begin{cases} \dot{V} = \frac{T\cos\alpha\cos\beta - D - mg\sin\gamma}{m}, \\ \dot{\chi} = \frac{T(\sin\alpha\sin\mu - \cos\alpha\sin\beta\cos\mu) + Y\cos\mu + L\sin\mu}{mV\cos\gamma}, \\ \dot{\gamma} = \frac{T(\sin\alpha\cos\mu + \cos\alpha\sin\beta\sin\mu) - Y\sin\mu + L\cos\mu - mg\cos\gamma}{mV}, \end{cases} \tag{4}$$

$$\begin{cases} \dot{\alpha} = q - p\cos\alpha\tan\beta - r\sin\alpha\tan\beta \\ \qquad - \frac{\cos\mu}{\cos\beta}\dot{\gamma} - \sin\mu\frac{\cos\gamma}{\cos\beta}\dot{\chi}, \\ \dot{\beta} = p\sin\alpha - r\cos\alpha - \sin\mu\dot{\gamma} + \cos\mu\cos\gamma\dot{\chi}, \\ \dot{\mu} = p\frac{\cos\alpha}{\cos\beta} + r\frac{\sin\alpha}{\cos\beta} + \cos\mu\tan\beta\dot{\gamma} \\ \qquad + (\sin\gamma + \sin\mu\cos\gamma\tan\beta)\dot{\chi}, \end{cases} \tag{5}$$

$$\begin{cases} \dot{p} = (c_1 r + c_2 p)q + c_3 M_l + c_4 M_n, \\ \dot{q} = c_5 pr - c_6\left(p^2 - r^2\right) + c_7 M_m, \\ \dot{r} = (c_8 p - c_2 r)q + c_4 M_l + c_9 M_n, \end{cases} \tag{6}$$

where the constants c_i ($i = 1, 2, \cdots, 9$) are defined as $c_1 = ((I_y - I_z)I_z - I_{xz}^2)/\Gamma$, $c_2 = ((I_x - I_y + I_z)I_{xz})/\Gamma$, $c_3 = I_z/\Gamma$, $c_4 = I_{xz}/\Gamma$, $c_5 = (I_z - I_x)/I_y$, $c_6 = I_{xz}/I_y$, $c_7 = 1/I_y$, $c_8 = (I_x(I_x - I_y) + I_{xz}^2)/\Gamma$, $c_9 = I_x/\Gamma$ with $\Gamma = I_x I_z - I_{xz}^2$. Note that the engine installation angle is zero, so the thrust line coincides with the body frame.

3. TRADITIONAL BACK-STEPPING CONTROLLER DESIGN

In this section, a traditional back-stepping controller is designed for this morphing aircraft. The TBC method is a systematic design approach for uncertain systems. The nonlinear system is divided into cascading subsystems, and the selection of a Lyapunov function and the design of the controller are combined to ensure the global stability of the closed-loop system [26–29].

For simplicity, the dynamic model in (5) and (6) can be written as

$$\begin{cases} \dot{\mathbf{x}}_1 = \mathbf{f}_1(\mathbf{x}_m) + \mathbf{g}_1(\mathbf{x}_m)\mathbf{x}_2 + \mathbf{g}_{1u}(\mathbf{x}_m)\mathbf{u}, \\ \dot{\mathbf{x}}_2 = \mathbf{f}_2(\mathbf{x}_n) + \mathbf{g}_2(\mathbf{x}_n)\mathbf{u}, \end{cases} \tag{7}$$

where the state and input vectors are defined as $\mathbf{x}_m = \begin{bmatrix} V & \gamma & \alpha & \beta & \mu \end{bmatrix}^{\mathrm{T}}$, $\mathbf{x}_n = \begin{bmatrix} V & \gamma & \alpha & \beta & \mu & p & q & r \end{bmatrix}^{\mathrm{T}}$, $\mathbf{u} = [\delta_{cs1R} \ \ \delta_{cs1L} \ \ \delta_{cs2R} \ \ \delta_{cs2L} \ \ \delta_{vcsR} \ \ \delta_{vcsL}]^{\mathrm{T}}$, $\mathbf{x}_1 = \begin{bmatrix} \alpha & \beta & \mu \end{bmatrix}^{\mathrm{T}}$, and $\mathbf{x}_2 = \begin{bmatrix} p & q & r \end{bmatrix}^{\mathrm{T}}$.

Assumption 1: The control surface deflection has negligible effects on the aerodynamic force [30,31], i.e., $\mathbf{g}_{1u}(\mathbf{x}_m)\mathbf{u} \approx 0$.

According to Assumption 1, the dynamic model can be rewritten as follows:

$$\begin{cases} \dot{\mathbf{x}}_1 = \mathbf{f}_1(\mathbf{x}_m) + \mathbf{g}_1(\mathbf{x}_m)\mathbf{x}_2, \\ \dot{\mathbf{x}}_2 = \mathbf{f}_2(\mathbf{x}_n) + \mathbf{g}_2(\mathbf{x}_n)\mathbf{u}, \end{cases} \tag{8}$$

where the functions $\mathbf{f}_i(\cdot)$ and $\mathbf{g}_i(\cdot)$ are given in Appendix A. Equation (8) denote two separate subsystems.

Assumption 2: The command signal $\mathbf{y}_{1d} = \mathbf{x}_{1d} = \begin{bmatrix} \alpha_d & \beta_d & \mu_d \end{bmatrix}^{\mathrm{T}}$ is bounded and continuously differentiable, and its first derivative ($\dot{\mathbf{x}}_{1d}$) is also bounded.

Assumption 3: The matrices $\mathbf{g}_1(\mathbf{x}_m) \in \mathbf{R}^{3\times3}$ and $\mathbf{g}_2(\mathbf{x}_n) \in \mathbf{R}^{3\times6}$ are invertible.

Remark 1: Assumption 1 is adopted in [30], in which numerical analysis finds that the control surfaces have a negligible influence on the aerodynamic force. Assumption 2 ensures that the command signal for aircraft control satisfies the conditions of continuous differentiability and a bounded first derivative. The model equations indicate that Assumption 3 is satisfied in general. If not, the pseudo-inverse can be used instead of the matrix inverse.

The specific steps of controller design are as follows:

Step 1: Design the control law of the first subsystem.

Define $\mathbf{e}_1$ as the tracking error of the first subsystem. Its derivative can be expressed as

$$\begin{cases} \mathbf{e}_1 = \mathbf{x}_1 - \mathbf{y}_{1d}, \\ \dot{\mathbf{e}}_1 = \dot{\mathbf{x}}_1 - \dot{\mathbf{y}}_{1d} \\ \qquad = \mathbf{f}_1(\mathbf{x}_m) + \mathbf{g}_1(\mathbf{x}_m)\mathbf{x}_2 - \dot{\mathbf{y}}_{1d}. \end{cases} \tag{9}$$

Define $\mathbf{x}_{2d} = \begin{bmatrix} p_d & q_d & r_d \end{bmatrix}^{\mathrm{T}}$ as the desired signal of the second subsystem. The virtual control law of the first system can then be designed as

$$\mathbf{x}_{2d} = \mathbf{g}_1(\mathbf{x}_m)^{-1}\left(\dot{\mathbf{y}}_{1d} - \mathbf{f}_1(\mathbf{x}_m) - \mathbf{K}_1\mathbf{e}_1\right), \tag{10}$$

where $\mathbf{K}_1 \in \mathbf{R}^{3\times3}$ is a diagonal positive-definite matrix.

Step 2: Design the control law of the second subsystem.

In this subsystem, the signal $\mathbf{x}_{2d}$ obtained by (10) is differentiated, which will cause the signal $\dot{\mathbf{y}}_{1d}$ to be differentiated again. Repeated differentiations may lead to the problem of differential explosion. Thus, the first-order filter $\mathbf{z}_2$ is introduced to avoid this problem. This filter is expressed as follows:

$$\boldsymbol{\tau}_2\dot{\mathbf{z}}_2+\mathbf{z}_2=\mathbf{x}_{2d},\ \ \mathbf{z}_2(0)=\mathbf{x}_{2d}(0), \tag{11}$$

where $\boldsymbol{\tau}_2\in\mathbf{R}^{3\times3}$ is a diagonal time-constant matrix.

Define $\mathbf{e}_2$ as the tracking error of the second subsystem. Its derivative can be expressed as

$$\begin{cases}\mathbf{e}_2=\mathbf{x}_2-\mathbf{z}_2,\\ \dot{\mathbf{e}}_2=\dot{\mathbf{x}}_2-\dot{\mathbf{z}}_2\\ \quad=\mathbf{f}_2(\mathbf{x}_n)+\mathbf{g}_2(\mathbf{x}_n)\mathbf{u}-\dot{\mathbf{z}}_2.\end{cases} \tag{12}$$

Thus, the control law for the second subsystem is given by

$$\mathbf{u}=\mathbf{g}_2(\mathbf{x}_n)^{-1}\left(\dot{\mathbf{z}}_2-\mathbf{f}_2(\mathbf{x}_n)-\mathbf{K}_2\mathbf{e}_2-\mathbf{g}_1^{\mathrm{T}}(\mathbf{x}_m)\mathbf{e}_1\right) \tag{13}$$

where $\mathbf{K}_2\in\mathbf{R}^{3\times3}$ is a diagonal positive-definite matrix.

4. ADAPTIVE BACK-STEPPING NEURAL CONTROLLER DESIGN

For the morphing aircraft, the model of motion is a nonlinear system with coupling between the morphing strategy and aerodynamic parameters. Additionally, external disturbances should be considered in the model. Therefore, it is difficult to model the aerodynamics precisely during the morphing process. In this section, an adaptive back-stepping neural controller is proposed. Based on the TBC method, neural networks are introduced to approximate unknown nonlinear functions. Thus, accurate prior knowledge of the aerodynamic parameters is no longer required.

4.1. Preliminaries and neural networks

Considering the modeling uncertainty and external interference, (8) can be written as

$$\begin{cases}\dot{\mathbf{x}}_1=\mathbf{f}_1(\mathbf{x}_m)+\mathbf{g}_1(\mathbf{x}_m)\mathbf{x}_2+\boldsymbol{\Delta}_1,\\ \dot{\mathbf{x}}_2=\mathbf{f}_2(\mathbf{x}_n)+\mathbf{g}_2(\mathbf{x}_n)\mathbf{u}+\boldsymbol{\Delta}_2,\end{cases} \tag{14}$$

where $\boldsymbol{\Delta}_1$ and $\boldsymbol{\Delta}_2$ denote the approximation errors in each subsystem, respectively. To deal with the system uncertainty in each subsystem effectively, RBF neural networks (NNs) are adopted.

Theorem 1 [32]**:** An arbitrary continuous function $\Delta\in\mathbb{R}$ can be approximated using an RBF NN. The expression is as follows:

$$\Delta=\boldsymbol{\omega}^{\mathrm{T}}\boldsymbol{\rho}+\varepsilon, \tag{15}$$

where $\mathbf{w}\in\mathbf{R}^N$ is the weight matrix of the NN ($N>1$ denotes the number of NN nodes), $\rho\in\mathbf{R}^N$ is the RBF matrix, and $\varepsilon\in\mathbb{R}$ denotes the approximation error of the NN.

Definition 1: The function $\mathrm{trv}(\mathbf{A})$ is defined to obtain the vectors of diagonal elements of the matrix $\mathbf{A}\in\mathbf{R}^{M\times M}$. $\mathrm{trv}(\mathbf{A})$ and $\mathbf{A}$ are defined as follows:

$$\begin{aligned}&\mathrm{trv}(\mathbf{A})=[a_{1,1},a_{2,2},\cdots,a_{M,M}]^{\mathrm{T}},\\ &\mathbf{A}=\begin{bmatrix}a_{1,1}&\cdots&a_{1,M}\\ \vdots&\ddots&\vdots\\ a_{M,1}&\cdots&a_{M,M}\end{bmatrix}.\end{aligned} \tag{16}$$

Remark 2: In this paper, $\boldsymbol{\Delta}_1$ and $\boldsymbol{\Delta}_2$ denote the approximation errors of the two subsystems, and are defined as follows:

$$\begin{cases}\mathbf{W}_1=[\boldsymbol{\omega}_1,\boldsymbol{\omega}_2,\boldsymbol{\omega}_3]\in\mathbf{R}^{N\times3},\\ \mathbf{P}_1=[\boldsymbol{\rho}_1,\boldsymbol{\rho}_2,\boldsymbol{\rho}_3]\in\mathbf{R}^{N\times3},\\ \boldsymbol{\varepsilon}_1=[\varepsilon_1,\varepsilon_2,\varepsilon_3]^{\mathrm{T}}\in\mathbf{R}^3,\end{cases} \tag{17}$$

$$\begin{aligned}\boldsymbol{\Delta}_1&=\begin{bmatrix}(\boldsymbol{\omega}_1)^{\mathrm{T}}\boldsymbol{\rho}_1(\mathbf{x}_{\mathrm{in}1})+\varepsilon_1\\ (\boldsymbol{\omega}_2)^{\mathrm{T}}\boldsymbol{\rho}_2(\mathbf{x}_{\mathrm{in}2})+\varepsilon_2\\ (\boldsymbol{\omega}_3)^{\mathrm{T}}\boldsymbol{\rho}_3(\mathbf{x}_{\mathrm{in}3})+\varepsilon_3\end{bmatrix}\\ &=\mathrm{trv}\left((\mathbf{W}_1)^{\mathrm{T}}\mathbf{P}_1\right)+\boldsymbol{\varepsilon}_1,\end{aligned} \tag{18}$$

$$\begin{cases}\mathbf{W}_2=[\boldsymbol{\omega}_4,\boldsymbol{\omega}_5,\boldsymbol{\omega}_6]\in\mathbf{R}^{N\times3},\\ \mathbf{P}_2=[\boldsymbol{\rho}_4,\boldsymbol{\rho}_5,\boldsymbol{\rho}_6]\in\mathbf{R}^{N\times3},\\ \boldsymbol{\varepsilon}_2=[\varepsilon_4,\varepsilon_5,\varepsilon_6]^{\mathrm{T}}\in\mathbf{R}^3,\end{cases} \tag{19}$$

$$\begin{aligned}\boldsymbol{\Delta}_2&=\begin{bmatrix}(\boldsymbol{\omega}_4)^{\mathrm{T}}\boldsymbol{\rho}_4(\mathbf{x}_{\mathrm{in}4})+\varepsilon_4\\ (\boldsymbol{\omega}_5)^{\mathrm{T}}\boldsymbol{\rho}_5(\mathbf{x}_{\mathrm{in}5})+\varepsilon_5\\ (\boldsymbol{\omega}_6)^{\mathrm{T}}\boldsymbol{\rho}_6(\mathbf{x}_{\mathrm{in}6})+\varepsilon_6\end{bmatrix}\\ &=\mathrm{trv}\left((\mathbf{W}_2)^{\mathrm{T}}\mathbf{P}_2\right)+\boldsymbol{\varepsilon}_2,\end{aligned} \tag{20}$$

where $\boldsymbol{\omega}_i=[\omega_{i,1},\omega_{i,2},\cdots,\omega_{i,N}]^{\mathrm{T}}\in\mathbf{R}^N$ $(i=1,\cdots,6)$ is the weight vector of the NN and $\boldsymbol{\rho}_i=[\rho_{i,1},\rho_{i,2},\cdots,\rho_{i,N}]^{\mathrm{T}}\in\mathbf{R}^N$ is the radial basis function vector, and $\mathbf{x}_{\mathrm{in}i}$ is the input vector of the NN (a detailed definition is given later).

The RBF $\rho_{i,j}(\mathbf{x}_{\mathrm{in}i})$ usually takes the form of a Gaussian function

$$\begin{aligned}&\rho_{i,j}(\mathbf{x}_{\mathrm{in}i})=\frac{1}{\sqrt{2\pi}\sigma_{i,j}}\exp\left(-\frac{\|\mathbf{x}_{\mathrm{in}i}-\boldsymbol{\zeta}_{\mathrm{in}i}\|^2}{2\sigma_{i,j}^2}\right),\\ &i=1,\cdots,6;\ \ j=1,\cdots,N,\end{aligned} \tag{21}$$

where $\boldsymbol{\zeta}_{\mathrm{in}i}$ is the center vector of the RBF and $\sigma_{i,j}$ is the jth RBF bandwidth. The specific definitions of $\mathbf{x}_{\mathrm{in}i}$ and $\boldsymbol{\zeta}_{\mathrm{in}i}$ are as follows:

$$\begin{cases}\mathbf{x}_{\mathrm{in}1}=[\alpha,\dot{\alpha},q]^{\mathrm{T}},\quad \boldsymbol{\zeta}_{\mathrm{in}1}=[\alpha_d,\dot{\alpha}_d,0]^{\mathrm{T}},\\ \mathbf{x}_{\mathrm{in}2}=[\beta,\dot{\beta},r]^{\mathrm{T}},\quad \boldsymbol{\zeta}_{\mathrm{in}2}=\left[\beta_d,\dot{\beta}_d,0\right]^{\mathrm{T}},\\ \mathbf{x}_{\mathrm{in}3}=[\mu,\dot{\mu},p]^{\mathrm{T}},\quad \boldsymbol{\zeta}_{\mathrm{in}3}=[\mu_d,\dot{\mu}_d,0]^{\mathrm{T}},\end{cases} \tag{22}$$

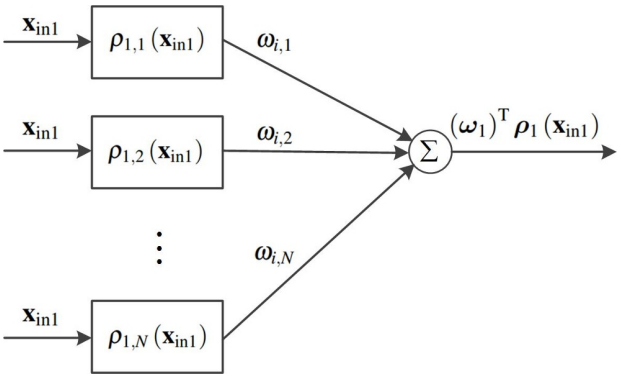

Fig. 5. Structure of NN.

$$\begin{cases} \mathbf{x}_{\text{in4}} = [p, \dot{p}]^{\mathrm{T}}, & \boldsymbol{\zeta}_{\text{in4}} = [p_d, \dot{p}_d]^{\mathrm{T}}, \\ \mathbf{x}_{\text{in5}} = [q, \dot{q}]^{\mathrm{T}}, & \boldsymbol{\zeta}_{\text{in5}} = [q_d, \dot{q}_d]^{\mathrm{T}}, \\ \mathbf{x}_{\text{in6}} = [r, \dot{r}]^{\mathrm{T}}, & \boldsymbol{\zeta}_{\text{in6}} = [r_d, \dot{r}_d]^{\mathrm{T}}. \end{cases} \tag{23}$$

Taking $(\boldsymbol{\omega}_1)^{\mathrm{T}}\boldsymbol{\rho}_1(\mathbf{x}_{\text{in1}})$ as an example, the structure of the NN is shown in Fig. 5.

4.2. Controller design

According to (14), the control law is redesigned as follows. The structure of the proposed control scheme is presented in Fig. 6. The specific steps of controller design are as follows:

Step : Design the control law of the first subsystem:

The tracking error is defined as $\mathbf{e}_1 = [e_1, e_2, e_3]^{\mathrm{T}} \in \mathbf{R}^3$ and $\mathbf{y}_{1d}$ is the desired command signal. The derivative of $\mathbf{e}_1$ can be expressed as

$$\begin{cases} \mathbf{e}_1 = \mathbf{x}_1 - \mathbf{y}_{1d}, \\ \dot{\mathbf{e}}_1 = \dot{\mathbf{x}}_1 - \dot{\mathbf{y}}_{1d}, \\ \quad = \mathbf{f}_1(\mathbf{x}_m) + \mathbf{g}_1(\mathbf{x}_m)\mathbf{x}_2 + \operatorname{trv}\left((\mathbf{W}_1)^{\mathrm{T}}\mathbf{P}_1\right) \\ \qquad + \boldsymbol{\varepsilon}_1 - \dot{\mathbf{y}}_{1d}. \end{cases} \tag{24}$$

Define $\mathbf{x}_{2d}$ as the desired signal of the second subsystem. The virtual control law of the first system can then be designed as

$$\begin{aligned} \mathbf{x}_{2d} = \mathbf{g}_1(\mathbf{x}_m)^{-1} \Big(& \dot{\mathbf{y}}_{1d} - \mathbf{f}_1(\mathbf{x}_m) - \mathbf{K}_1\mathbf{e}_1 \\ & - \operatorname{trv}\left((\hat{\mathbf{W}}_1)^{\mathrm{T}}\mathbf{P}_1\right) \Big), \end{aligned} \tag{25}$$

where $\mathbf{K}_1 \in \mathbf{R}^{3\times 3}$ is a diagonal positive-definite matrix and $\hat{\mathbf{W}}_1 = [\hat{\boldsymbol{\omega}}_1, \hat{\boldsymbol{\omega}}_2, \hat{\boldsymbol{\omega}}_3]^{\mathrm{T}} \in \mathbf{R}^{N\times 3}$ is the weight matrix of the NN.

The updated law for $\hat{\boldsymbol{\omega}}_i$ is given by

$$\dot{\hat{\boldsymbol{\omega}}}_i = \boldsymbol{\Gamma}_i(\boldsymbol{\rho}_i e_i - \eta_i \hat{\boldsymbol{\omega}}_i), \quad i = 1,2,3, \tag{26}$$

where $\boldsymbol{\Gamma}_i \in \mathbf{R}^{N\times N}$ is a diagonal positive-definite matrix and η_i is a positive design constant.

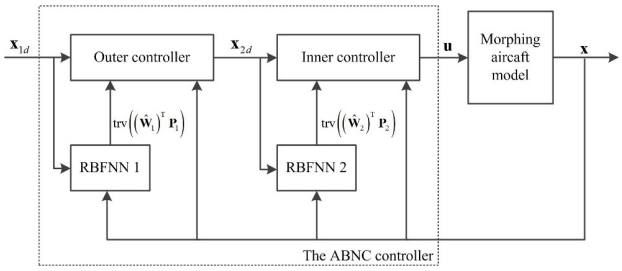

Fig. 6. Controller scheme.

Step 2: Design the control law of the second subsystem:

To prevent the problem of differential explosion, a first-order filter $\mathbf{z}_2$ is introduced.

$$\boldsymbol{\tau}_2\dot{\mathbf{z}}_2 + \mathbf{z}_2 = \mathbf{x}_{2d}, \quad \mathbf{z}_2(0) = \mathbf{x}_{2d}(0), \tag{27}$$

where $\boldsymbol{\tau}_2 \in \mathbf{R}^{3\times 3}$ is a diagonal time-constant matrix.

Define $\mathbf{e}_2 = [e_4, e_5, e_6]^{\mathrm{T}} \in \mathbf{R}^3$ as the tracking error of the second subsystem. Its derivative can be expressed as

$$\begin{cases} \mathbf{e}_2 = \mathbf{x}_2 - \mathbf{z}_2, \\ \dot{\mathbf{e}}_2 = \dot{\mathbf{x}}_2 - \dot{\mathbf{z}}_2 \\ \quad = \mathbf{f}_2(\mathbf{x}_n) + \mathbf{g}_2(\mathbf{x}_n)\mathbf{u} + \operatorname{trv}\left((\mathbf{W}_2)^{\mathrm{T}}\mathbf{P}_2\right) \\ \qquad + \boldsymbol{\varepsilon}_2 - \dot{\mathbf{z}}_2. \end{cases} \tag{28}$$

Thus, the control law for the second subsystem is given by

$$\begin{aligned} \mathbf{u} = \mathbf{g}_2(\mathbf{x}_n)^{-1} \Big(& \dot{\mathbf{z}}_2 - \mathbf{f}_2(\mathbf{x}_n) - \mathbf{K}_2\mathbf{e}_2 \\ & - \operatorname{trv}\left((\hat{\mathbf{W}}_2)^{\mathrm{T}}\mathbf{P}_2\right) - \mathbf{g}_1^T(\mathbf{x}_m)\mathbf{e}_1 \Big), \end{aligned} \tag{29}$$

where $\mathbf{K}_2 \in \mathbf{R}^{3\times 3}$ is a diagonal positive-definite matrix and $\hat{\mathbf{W}}_2 = [\hat{\boldsymbol{\omega}}_4, \hat{\boldsymbol{\omega}}_5, \hat{\boldsymbol{\omega}}_6]^{\mathrm{T}} \in \mathbf{R}^{N\times 3}$ is the weight matrix of the NN. The updated law is given by

$$\dot{\hat{\boldsymbol{\omega}}}_i = \boldsymbol{\Gamma}_i(\boldsymbol{\rho}_i e_i - \eta_i \hat{\boldsymbol{\omega}}_i), \quad i = 4,5,6, \tag{30}$$

where $\boldsymbol{\Gamma}_i \in \mathbf{R}^{N\times N}$ is a diagonal positive-definite matrix and η_i is a positive design constant.

After introducing the first-order filter and improving the control law, it is necessary to prove the stability of the controller.

4.3. Stability analysis

Define the errors as follows:

$$\begin{cases} \tilde{\mathbf{W}}_i = \mathbf{W}_i - \hat{\mathbf{W}}_i, \quad i = 1,2, \\ \tilde{\boldsymbol{\omega}}_j = \boldsymbol{\omega}_j - \hat{\boldsymbol{\omega}}_j, \quad j = 1,\cdots,6, \\ \mathbf{e}_{z2} = \mathbf{z}_2 - \mathbf{x}_{2d}. \end{cases} \tag{31}$$

Substituting these into (27) yields

$$\dot{\mathbf{z}}_2 = \boldsymbol{\tau}_2^{-1}(\mathbf{x}_{2d} - \mathbf{z}_2) = -\boldsymbol{\tau}_2^{-1}\mathbf{e}_{z2}. \tag{32}$$

Therefore, the derivative of $\mathbf{e}_{z2}$ can be obtained as

$$\begin{cases} \dot{\mathbf{e}}_{z2} = -\boldsymbol{\tau}_2^{-1}\mathbf{e}_{z2} - \mathbf{b}_2(\cdot), \\ \mathbf{b}_2(\cdot) = \dot{\mathbf{x}}_{2d}. \end{cases} \tag{33}$$

Because the aerodynamic parameters of the aircraft are bounded, the deflection of the control surface is limited, and the above functions are all continuous functions. Hence, $\mathbf{b}_2(\cdot)$ is continuous, and has the following maximum F-norm:

$$\|\mathbf{b}_2(\cdot)\|_{\max} = b_{2\max}. \tag{34}$$

Definition 2: The F-norm (Frobenius norm) of a matrix or vector $\mathbf{A}$ is $\|\mathbf{A}\| = \sqrt{tr(\mathbf{A}^{\mathrm{T}}\mathbf{A})}$.

Definition 3: Young's inequality is defined as

$$\mathbf{a}^{\mathrm{T}}\mathbf{b} \le \frac{1}{2}\left(\|\mathbf{a}\|^2 + \|\mathbf{b}\|^2\right). \tag{35}$$

Lemma 1 (Young's inequality [33,34])**:** For $\|\mathbf{A}\| \le a_{\max}$, $a_{\max} > 0$, the following inequality holds:

$$\begin{aligned} \mathbf{a}^{\mathrm{T}}\mathbf{A}\mathbf{b} &\le a_{\max}\|\mathbf{a}\|\|\mathbf{b}\| \\ &\le a_{\max}\left(\|\mathbf{a}\|^2 + \frac{\|\mathbf{b}\|^2}{4}\right). \end{aligned} \tag{36}$$

For convenience, in the following, abbreviations such as $\mathbf{f}_1$ are used for $\mathbf{f}_1(\mathbf{x}_m)$. Combining the above equations, we obtain

$$\begin{aligned} \dot{\mathbf{e}}_1 &= \mathbf{f}_1 + \mathbf{g}_1\mathbf{x}_2 + \mathrm{trv}\left((\mathbf{W}_1)^{\mathrm{T}}\mathbf{P}_1\right) + \boldsymbol{\varepsilon}_1 - \dot{\mathbf{y}}_{1d} \\ &= \mathbf{f}_1 + \mathbf{g}_1(\mathbf{x}_2 - \mathbf{z}_2 + \mathbf{z}_2 - \mathbf{x}_{2d} + \mathbf{x}_{2d}) \\ &\quad + \mathrm{trv}\left((\mathbf{W}_1)^{\mathrm{T}}\mathbf{P}_1\right) + \boldsymbol{\varepsilon}_1 - \dot{\mathbf{y}}_{1d} \\ &= \mathbf{g}_1(\mathbf{e}_2 + \mathbf{e}_{z2}) - \mathbf{K}_1\mathbf{e}_1 + \mathrm{trv}\left((\tilde{\mathbf{W}}_1)^{\mathrm{T}}\mathbf{P}_1\right) + \boldsymbol{\varepsilon}_1, \end{aligned} \tag{37}$$

$$\begin{aligned} \dot{\mathbf{e}}_2 &= \mathbf{f}_2 + \mathbf{g}_2\mathbf{u} + \mathrm{trv}\left((\mathbf{W}_2)^{\mathrm{T}}\mathbf{P}_2\right) + \boldsymbol{\varepsilon}_2 - \dot{\mathbf{z}}_2 \\ &= -\mathbf{K}_2\mathbf{e}_2 - \mathbf{g}_1^T\mathbf{e}_1 + \mathrm{trv}\left((\tilde{\mathbf{W}}_2)^{\mathrm{T}}\mathbf{P}_2\right) + \boldsymbol{\varepsilon}_2. \end{aligned} \tag{38}$$

Consider the following Lyapunov function:

$$\begin{cases} L_v = L_{v1} + L_{v2}, \\ L_{v1} = \frac{1}{2}\mathbf{e}_1^T\mathbf{e}_1 + \frac{1}{2}\mathbf{e}_{z2}^T\mathbf{e}_{z2} + \frac{1}{2}\sum_{i=1}^{3}\tilde{\boldsymbol{\omega}}_i^{\mathrm{T}}\boldsymbol{\Gamma}_i^{-1}\tilde{\boldsymbol{\omega}}_i, \\ L_{v2} = \frac{1}{2}\mathbf{e}_2^T\mathbf{e}_2 + \frac{1}{2}\sum_{i=4}^{6}\tilde{\boldsymbol{\omega}}_i^{\mathrm{T}}\boldsymbol{\Gamma}_i^{-1}\tilde{\boldsymbol{\omega}}_i. \end{cases} \tag{39}$$

From (26) and (30), we can infer that $\dot{\tilde{\boldsymbol{\omega}}}_i = -\dot{\hat{\boldsymbol{\omega}}}_i$. Hence, $\dot{L}_{v1}$ and $\dot{L}_{v2}$ are expressed as

$$\begin{aligned} \dot{L}_{v1} &= \mathbf{e}_1^{\mathrm{T}}\dot{\mathbf{e}}_1 + \mathbf{e}_{z2}^{\mathrm{T}}\dot{\mathbf{e}}_{z2} - \sum_{i=1}^{3}\tilde{\boldsymbol{\omega}}_i^{\mathrm{T}}\boldsymbol{\Gamma}_i^{-1}\dot{\hat{\boldsymbol{\omega}}}_i \\ &= \mathbf{e}_1^{\mathrm{T}}\mathbf{g}_1(\mathbf{e}_2 + \mathbf{e}_{z2}) - \mathbf{e}_1^{\mathrm{T}}\mathbf{K}_1\mathbf{e}_1 + \mathbf{e}_1^{\mathrm{T}}\boldsymbol{\varepsilon}_1 \\ &\quad - \mathbf{e}_{z2}^{\mathrm{T}}\boldsymbol{\tau}_2^{-1}\mathbf{e}_{z2} - \mathbf{e}_{z2}^{\mathrm{T}}\mathbf{b}_2 + \mathbf{e}_1^{\mathrm{T}}\,\mathrm{trv}\left((\tilde{\mathbf{W}}_1)^{\mathrm{T}}\mathbf{P}_1\right) \\ &\quad - \sum_{i=1}^{3}\tilde{\boldsymbol{\omega}}_i^{\mathrm{T}}(\boldsymbol{\rho}_i e_i - \eta_i\hat{\boldsymbol{\omega}}_i), \end{aligned} \tag{40}$$

$$\begin{aligned} \dot{L}_{v2} &= \mathbf{e}_2^{\mathrm{T}}\dot{\mathbf{e}}_2 - \sum_{i=4}^{6}\tilde{\boldsymbol{\omega}}_i^{\mathrm{T}}\boldsymbol{\Gamma}_i^{-1}\dot{\hat{\boldsymbol{\omega}}}_i \\ &= -\mathbf{e}_2^{\mathrm{T}}\mathbf{K}_2\mathbf{e}_2 - \mathbf{e}_2^{\mathrm{T}}\mathbf{g}_1^T\mathbf{e}_1 + \mathbf{e}_2^{\mathrm{T}}\,\mathrm{trv}\left((\tilde{\mathbf{W}}_2)^{\mathrm{T}}\mathbf{P}_2\right) \\ &\quad + \mathbf{e}_2^{\mathrm{T}}\boldsymbol{\varepsilon}_2 - \sum_{i=4}^{6}\tilde{\boldsymbol{\omega}}_i^{\mathrm{T}}(\boldsymbol{\rho}_i e_i - \eta_i\hat{\boldsymbol{\omega}}_i). \end{aligned} \tag{41}$$

According to the matrix operation principle, the following expressions can be obtained:

$$\begin{cases} \mathbf{e}_1^{\mathrm{T}}\,\mathrm{trv}\left((\tilde{\mathbf{W}}_1)^{\mathrm{T}}\mathbf{P}_1\right) = \sum_{i=1}^{3}\tilde{\boldsymbol{\omega}}_i^{\mathrm{T}}\boldsymbol{\rho}_i e_i, \\ \mathbf{e}_2^{\mathrm{T}}\,\mathrm{trv}\left((\tilde{\mathbf{W}}_2)^{\mathrm{T}}\mathbf{P}_2\right) = \sum_{i=4}^{6}\tilde{\boldsymbol{\omega}}_i^{\mathrm{T}}\rho_i e_i. \end{cases} \tag{42}$$

Substituting (42) into (40) and (41) yields

$$\begin{aligned} \dot{L}_{v1} &= \mathbf{e}_1^{\mathrm{T}}\mathbf{g}_1\mathbf{e}_2 + \mathbf{e}_1^{\mathrm{T}}\mathbf{g}_1\mathbf{e}_{z2} - \mathbf{e}_1^{\mathrm{T}}\mathbf{K}_1\mathbf{e}_1 + \mathbf{e}_1^{\mathrm{T}}\boldsymbol{\varepsilon}_1 \\ &\quad - \mathbf{e}_{z2}^{\mathrm{T}}\boldsymbol{\tau}_2^{-1}\mathbf{e}_{z2} - \mathbf{e}_{z2}^{\mathrm{T}}\mathbf{b}_2 + \sum_{i=1}^{3}\eta_i\tilde{\boldsymbol{\omega}}_i^{\mathrm{T}}\hat{\boldsymbol{\omega}}_i, \\ \dot{L}_{v2} &= -\mathbf{e}_2^{\mathrm{T}}\mathbf{K}_2\mathbf{e}_2 - \mathbf{e}_2^{\mathrm{T}}\mathbf{g}_1^T\mathbf{e}_1 + \mathbf{e}_2^{\mathrm{T}}\boldsymbol{\varepsilon}_2 + \sum_{i=4}^{6}\eta_i\tilde{\boldsymbol{\omega}}_i^{\mathrm{T}}\hat{\boldsymbol{\omega}}_i. \end{aligned} \tag{43}$$

Then, from (31), we find that

$$\begin{aligned} \sum_{i=1}^{3}\tilde{\boldsymbol{\omega}}_i^{\mathrm{T}}\hat{\boldsymbol{\omega}}_i &\le \frac{1}{2}\sum_{i=1}^{3}\left(\|\boldsymbol{\omega}_i\|^2 - \|\tilde{\boldsymbol{\omega}}_i\|^2\right), \\ \sum_{i=4}^{6}\tilde{\boldsymbol{\omega}}_i^{\mathrm{T}}\hat{\boldsymbol{\omega}}_i &\le \frac{1}{2}\sum_{i=4}^{6}\left(\|\boldsymbol{\omega}_i\|^2 - \|\tilde{\boldsymbol{\omega}}_i\|^2\right). \end{aligned} \tag{44}$$

Note that $\|\mathbf{g}_1\| \le g_{1\max}$, $\eta_i \le \eta_{\max}$ and $\lambda_{\min}(\mathbf{K}_1)$, $\lambda_{\min}(\mathbf{K}_2)$, $\lambda_{\min}(\boldsymbol{\tau}_2^{-1})$, and $\lambda_{\min}(\boldsymbol{\Gamma}_i)$ denote the minimum eigenvalues of the corresponding matrices. Additionally, $\lambda_{\min}(\boldsymbol{\Gamma}_i) \ge \lambda_{\min\Gamma}$ $(i = 1, \cdots, 6)$.

Therefore, (39) can be reformulated as

$$\begin{aligned} \dot{L}_v &= \dot{L}_{v1} + \dot{L}_{v2} \\ &= \mathbf{e}_1^{\mathrm{T}}\mathbf{g}_1\mathbf{e}_2 + \mathbf{e}_1^{\mathrm{T}}\mathbf{g}_1\mathbf{e}_{z2} - \mathbf{e}_1^{\mathrm{T}}\mathbf{K}_1\mathbf{e}_1 + \mathbf{e}_1^{\mathrm{T}}\boldsymbol{\varepsilon}_1 - \mathbf{e}_{z2}^{\mathrm{T}}\boldsymbol{\tau}_2^{-1}\mathbf{e}_{z2} \\ &\quad - \mathbf{e}_{z2}^{\mathrm{T}}\mathbf{b}_2 - \mathbf{e}_2^{\mathrm{T}}\mathbf{K}_2\mathbf{e}_2 - \mathbf{e}_2^{\mathrm{T}}\mathbf{g}_1^{\mathrm{T}}\mathbf{e}_1 + \mathbf{e}_2^{\mathrm{T}}\boldsymbol{\varepsilon}_2 + \sum_{i=1}^{6}\eta_i\tilde{\boldsymbol{\omega}}_i^{\mathrm{T}}\hat{\boldsymbol{\omega}}_i \\ &\le g_{1\max}\left(\|\mathbf{e}_1\|^2 + \frac{\|\mathbf{e}_{z2}\|^2}{4}\right) - \lambda_{\min}(\mathbf{K}_1)\mathbf{e}_1^T\mathbf{e}_1 \\ &\quad + \frac{1}{2}\|\mathbf{e}_1\|^2 + \frac{1}{2}\|\boldsymbol{\varepsilon}_1\|^2 - \frac{1}{2}\|\mathbf{e}_{z2}\|^2 - \frac{1}{2}b_{2\max}^2 \\ &\quad - \lambda_{\min}(\boldsymbol{\tau}_2^{-1})\mathbf{e}_{z2}^T\mathbf{e}_{z2} + \frac{\eta_{\max}}{2}\sum_{i=1}^{6}\left(\|\boldsymbol{\omega}_i\|^2 - \|\tilde{\boldsymbol{\omega}}_i\|^2\right) \end{aligned}$$

$$
\begin{aligned}
&-\lambda_{\min}(\mathbf{K}_2)\mathbf{e}_2^T\mathbf{e}_2+\frac{1}{2}\|\mathbf{e}_2\|^2+\frac{1}{2}\|\boldsymbol{\varepsilon}_2\|^2\\
\le&-\left(\lambda_{\min}(\mathbf{K}_1)-g_{1\max}-\frac{1}{2}\right)\mathbf{e}_1^T\mathbf{e}_1-\left(\lambda_{\min}(\boldsymbol{\tau}_2^{-1})\right.\\
&\left.-\frac{g_{1\max}}{4}+\frac{1}{2}\right)\mathbf{e}_{z2}^T\mathbf{e}_{z2}-\left(\lambda_{\min}(\mathbf{K}_2)-\frac{1}{2}\right)\mathbf{e}_2^T\mathbf{e}_2\\
&-\frac{\eta_{\max}\lambda_{\min\Gamma}}{2}\sum_{i=1}^{6}\left(\tilde{\boldsymbol{\omega}}_i^{\mathrm{T}}\boldsymbol{\Gamma}_i^{-1}\tilde{\boldsymbol{\omega}}_i\right)+\frac{1}{2}\|\boldsymbol{\varepsilon}_1\|^2\\
&-\frac{1}{2}b_{2\max}^2+\frac{1}{2}\|\boldsymbol{\varepsilon}_2\|^2+\frac{\eta_{\max}}{2}\sum_{i=1}^{6}\|\boldsymbol{\omega}_i\|^2\\
\le&-r_1L_v+r_2,
\end{aligned}
\tag{45}
$$

where

$$
\begin{cases}
r_1=2\min\left\{\lambda_{\min}(\mathbf{K}_1)-g_{1\max}-\dfrac{1}{2},\dfrac{\eta_{\max}\lambda_{\min\Gamma}}{2},\right.\\
\qquad\left.\lambda_{\min}(\mathbf{K}_2)-\dfrac{1}{2},\lambda_{\min}(\boldsymbol{\tau}_2^{-1})-\dfrac{g_{1\max}}{4}+\dfrac{1}{2}\right\},\\
r_2=\dfrac{1}{2}\left(\|\boldsymbol{\varepsilon}_1\|^2-b_{2\max}^2+\|\boldsymbol{\varepsilon}_2\|^2+\eta_{\max}\sum_{i=1}^{6}\|\boldsymbol{\omega}_i\|^2\right).
\end{cases}
\tag{46}
$$

Integrating (45) on the interval $[0, t]$ gives

$$
L_v(t)\le\left[L_v(0)-\frac{r_2}{r_1}\right]e^{-r_1t}+\frac{r_2}{r_1}.
\tag{47}
$$

According to (39), we have

$$
\mathbf{e}_1^T\mathbf{e}_1\le 2L_v.
\tag{48}
$$

Thus, the scope of the tracking error can be written as follows:

$$
\|\mathbf{e}_1\|\le\sqrt{2\left(\left[L_v(0)-\frac{r_2}{r_1}\right]e^{-r_1t}+\frac{r_2}{r_1}\right)}.
\tag{49}
$$

Selecting an appropriate parameter r_1 such that $r_1>0$, the designed control law ensures that the tracking error of the closed-loop system converges uniformly within the scope of (49).

5. SIMULATION RESULTS

To demonstrate the performance and robustness of the proposed ABNC method, three sets of simulation experiments are devised. The first two scenarios compare the simulation results of the ABNC method and the TBC method under fixed and variable V-tail conditions, respectively. To further illustrate the advantages of the ABNC method, aerodynamic uncertainty and wind disturbance are considered in the third simulation scenario. Using the classic PID control approach is applied to design the velocity controller, the control law is expressed as follows:

$$
\begin{cases}
\Delta T=K_v\Delta V+K_{vi}\int\Delta V\,dt,\\
\Delta V=V_d-V,
\end{cases}
\tag{50}
$$

where V_d is the velocity command, $K_v=20$, and $K_{vi}=0.01$.

The common control parameters of the two controllers are $\mathbf{K}_1=diag(4,\ 4,\ 4)$, $\mathbf{K}_2=diag(10,\ 10,\ 10)$, $\boldsymbol{\tau}_2=diag(0.01,\ 0.01,\ 0.01)$. For the proposed ABNC controller, each control channel is set up with 50 neural network nodes ($N=50$).

For the first subsystem, the NN weight elements $\omega_{i,j}$ ($i=1,2,3$, $j=1,\cdots,50$) in (18) are initially set to random values in the range [0, 1]. The corresponding RBF bandwidths $\sigma_{i,j}$ ($i=1,\ 2,\ 3,\ j=1,\cdots,50$) are evenly spaced in the interval [3, 4]. The parameters of the NN weight update law are set to $\boldsymbol{\Gamma}_1=\boldsymbol{\Gamma}_3=diag(100,\cdots,100)\in\mathbf{R}^{50\times50}$, $\boldsymbol{\Gamma}_2=diag(40,\ \cdots,\ 40)\in\mathbf{R}^{50\times50}$, $\eta_1=1$, $\eta_2=2.5$, and $\eta_3=1$.

For the second subsystem, the NN weight elements $\omega_{i,j}$ ($i=4,5,6$, $j=1,\cdots,50$) in (20) are initially set to random values in [0, 1]. The corresponding RBF bandwidths $\sigma_{i,j}$ ($i=4,5,6$, $j=1,\cdots,50$) are evenly spaced in the interval [20, 21]. The parameters of the NN weight update law are set to $\eta_i=1$ and $\boldsymbol{\Gamma}_i=diag(100,\cdots,100)\in\mathbf{R}^{50\times50}$ ($i=4,5,6$).

5.1. Simulation under the static V-tail condition

In this scenario, the angle of the V-tail is fixed at 30 degrees, and the initial trim conditions are $V_0=41.67$ m/s, $h_0=1000$ m, $\alpha_0=4.85^\circ$, $\beta_0=0^\circ$, and $\mu_0=0^\circ$. In this flight state, four comparative cases are designed to illustrate the effectiveness of the controller. Cases 1, 2, and 3 apply the desired signal to different channels separately, with the remaining channels unchanged. Case 4 applies the desired signals to three channels at the same time. The desired signal is written as follows:

$$
\Delta S_d=\begin{cases}5, & 5<t<10,\\ 0, & \text{else}.\end{cases}
\tag{51}
$$

Figs. 7(a)–7(c) demonstrate the performance of these two controllers for tracking the desired α, β, and μ commands. In Case 1, the settling times of the TBC and ABNC controllers on the α channel are 1.38 s and 0.74 s, respectively. The root mean square errors (RMSEs) are 0.861 and 0.701, respectively. In Case 2, the settling times of the TBC and ABNC controllers on the β channel are 1.22 s and 0.82 s, respectively, with RMSEs of 0.861 and 0.701. In Case 3, the settling times on the μ channel are 1.10 s and 0.66 s for the TBC controller and the ABNC controller, respectively, and the respective RMSEs are 0.855 and 0.676.

To further compare the two methods, the settling times and RMSEs for Case 4 are presented in Figs. 7(d) and 8, respectively. These results suggest that the ABNC controller reduces the settling time and decreases the RMSE under the static V-tail condition.

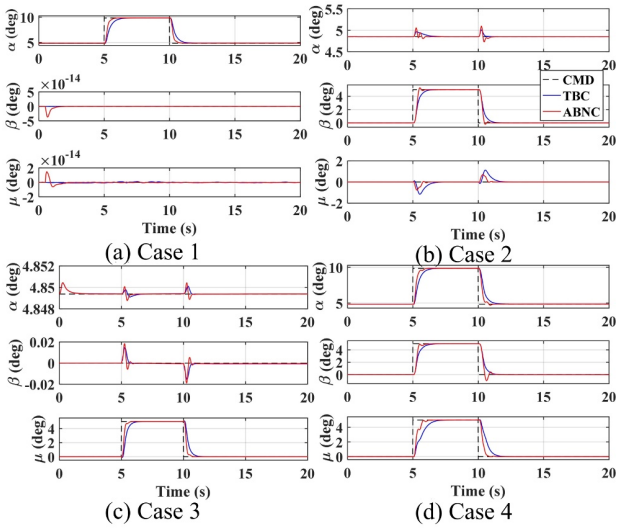

Fig. 7. Tracking performance in different Cases.

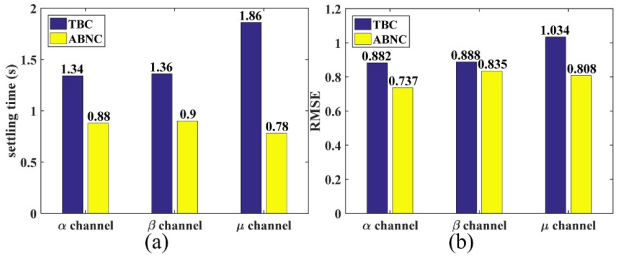

Fig. 8. Settling time and RMSE in Case 4.

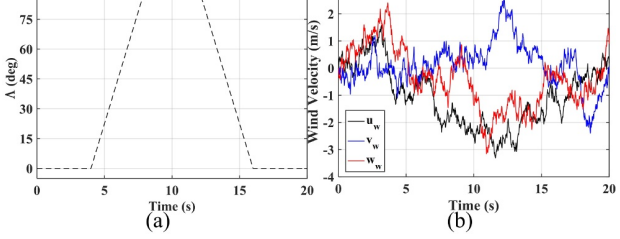

Fig. 9. V-tail switch signal and wind velocity.

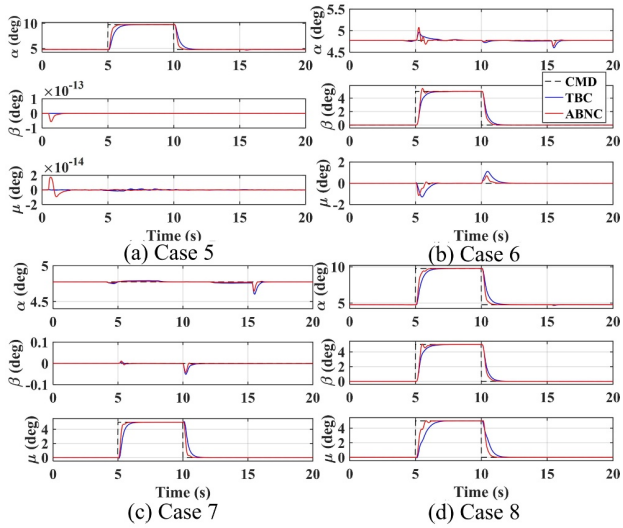

Fig. 10. Tracking performance in different Cases.

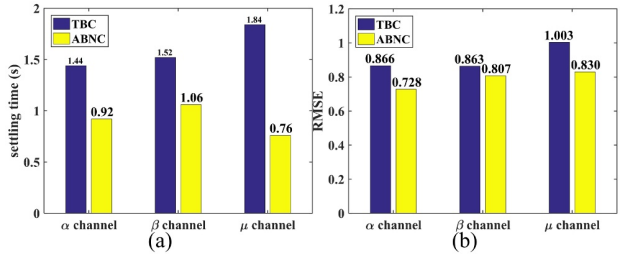

Fig. 11. Settling time and RMSE in Case 8.

5.2. Simulation under the dynamic V-tail condition

In this scenario, the V-tail angle is variable and changes as shown in Fig. 9(a). The initial trim conditions are $V_0 = 41.67$ m/s, $h_0 = 1000$ m, $\Lambda_0 = 0°$, $\alpha_0 = 4.85°$, $\beta_0 = 0°$, and $\mu_0 = 0°$. In this flight state, we again use four cases to compare the performance of the two controllers, as shown in Fig. 10.

Cases 5-8 used the same command signals as Cases 1-4, which is shown in (51). In Case 5, the settling times of the TBC controller and the ABNC controller on the α channel are 1.46 s and 0.74 s, respectively, and the RMSEs are 0.861 and 0.708, respectively. In Case 6, the settling times of the TBC controller and the ABNC controller on the β channel are 1.36 s and 0.88 s, respectively, with corresponding RMSEs of 0.858 and 0.801. In Case 7, the settling times of the TBC and ABNC controllers on the μ channel are 1.10 s and 0.66 s, respectively, and the respective RMSEs are 0.858 and 0.677. The signal tracking of Case 8 is shown in Fig. 10(d), and its settling times and RMSEs are shown in Fig. 11. As shown in these figures, the ABNC method achieves better performance than the TBC method in terms of both rapidity and accuracy.

5.3. Simulation with aerodynamics and wind uncertainties

The uncertainties of the wind and aerodynamic coefficients can impact the efficiency and effectiveness of the controllers. Thus, the aerodynamic coefficient variation and wind disturbance are taken into consideration in Case 9 (other simulation conditions are the same as in Case 8). The Dryden Wind Turbulence Model in Simulink is used as the wind model. This model uses the Dryden spectral representation to add turbulence to the aerospace model by passing band-limited white noise through appropriate forming filters. The mathematical representation uses Military Specification MIL-F-8785C. The wind velocities de-

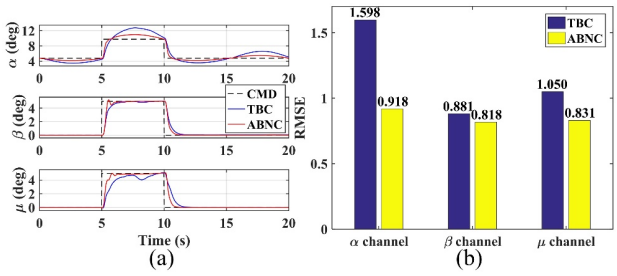

Fig. 12. Tracking performance and RMSE in Case 9.

noted in the three body axes are u_w, v_w, and w_w, as shown in Fig. 9(b). The aerodynamic coefficient variation is expressed as:

$$C_* = C_* \cdot (1 + 0.5\sin(0.2\pi t)), \quad * = \{D, Y, L\}. \tag{52}$$

As can be seen from Fig. 12(a), the ABNC controller offers superior robustness and performance to that of the TBC controller. The RMSEs shown in Fig. 12(b) support this conclusion.

6. CONCLUSIONS

This paper has analyzed the aerodynamic characteristics of a morphing aircraft with a variable V-tail. An adaptive back-stepping controller using online learning neural networks was designed. The longitudinal and lateral channel flight controllers were designed by the TBC method and the ABNC method, respectively. Using Lyapunov theory, the parameter ranges of the proposed method were derived and the Lyapunov stability for the proposed methods was proved. To compare the performance of the two methods in terms of rapidity, accuracy, and robustness, nine simulation cases across three scenarios were designed. The results show that the ABNC method works well with good tracking performance and robustness. In future work, we will focus on the morphing control policy for different missions and flight conditions using reinforcement learning techniques.

APPENDIX A

$$\begin{cases} D = C_D QS, \\ Y = C_Y QS, \\ L = C_L QS, \end{cases} \quad \begin{cases} M_l = C_l QSb, \\ M_m = C_m QSc_A, \\ M_n = C_n QSb, \end{cases} \tag{A.1}$$

$$\mathbf{f}_1(\mathbf{x}_m) = \begin{bmatrix} f_\alpha & f_\beta & f_\mu \end{bmatrix}^T, \tag{A.2}$$

where

$$\begin{cases} f_\alpha = \dfrac{1}{mV\cos\beta}(-L + mg\cos\gamma\cos\mu - T\sin\alpha), \\ f_\beta = \dfrac{1}{mV}(-T\cos\alpha\sin\beta + Y + mg\cos\gamma\sin\mu), \\ f_\mu = \dfrac{L}{mV}(\tan\beta + \tan\gamma\sin\mu) \\ \quad + \dfrac{1}{mV}(Y\cos\mu\tan\gamma - mg\cos\gamma\cos\mu\tan\beta) \\ \quad + \dfrac{T\sin\alpha}{mV}(\tan\beta + \sin\mu\tan\gamma) \\ \quad - \dfrac{T}{mV}\cos\alpha\sin\beta\cos\mu\tan\gamma, \end{cases}$$

$$\begin{cases} \mathbf{g}_1(\mathbf{x}_m) = \begin{bmatrix} -\cos\alpha\tan\beta & 1 & -\sin\alpha\tan\beta \\ \sin\alpha & 0 & -\cos\alpha \\ \frac{\cos\alpha}{\cos\beta} & 0 & \frac{\sin\alpha}{\cos\beta} \end{bmatrix}, \\ \mathbf{f}_2(\mathbf{x}_n) = \begin{bmatrix} f_p & f_q & f_r \end{bmatrix}^T, \end{cases} \tag{A.3}$$

where

$$\begin{cases} f_p = (c_1 r + c_2 p) q + c_3 QSb\left(C_l^\beta \beta + \dfrac{bC_l^p p}{2V} + \dfrac{bC_l^r r}{2V}\right) \\ \quad + c_4 QSb\left(C_n^\beta \beta + \dfrac{bC_n^p p}{2V} + \dfrac{bC_n^r r}{2V}\right), \\ f_q = c_5 pr - c_6(p^2 - r^2) + c_7 QSc_A\left(C_{mstatic} + \dfrac{c_A C_m^q q}{2V}\right), \\ f_r = (c_8 p - c_2 r) q + c_4 QSb\left(C_l^\beta \beta + \dfrac{bC_l^p p}{2V} + \dfrac{bC_l^r r}{2V}\right) \\ \quad + c_9 QSb\left(C_n^\beta \beta + \dfrac{bC_n^p p}{2V} + \dfrac{bC_n^r r}{2V}\right), \end{cases}$$

$$\mathbf{g}_2(\mathbf{x}_n) = \begin{bmatrix} g_{11} & g_{12} & g_{13} & g_{14} & g_{15} & g_{16} \\ g_{21} & g_{22} & g_{23} & g_{24} & g_{25} & g_{26} \\ g_{31} & g_{32} & g_{33} & g_{34} & g_{35} & g_{36} \end{bmatrix}, \tag{A.4}$$

where

$$\begin{cases} g_{11} = QSb\left(c_3 C_l^{cs1R} + c_4 C_n^{cs1R}\right), \\ g_{12} = QSb\left(c_3 C_l^{cs1L} + c_4 C_n^{cs1L}\right), \\ g_{13} = QSb\left(c_3 C_l^{cs2R} + c_4 C_n^{cs2R}\right), \\ g_{14} = QSb\left(c_3 C_l^{cs2L} + c_4 C_n^{cs2L}\right), \\ g_{15} = QSb\left(c_3 C_l^{vcsR} + c_4 C_n^{vcsR}\right), \\ g_{16} = QSb\left(c_3 C_l^{vcsL} + c_4 C_n^{vcsL}\right), \end{cases}$$

$$\begin{cases} g_{21} = QSc_A c_7 C_m^{cs1R}, \\ g_{22} = QSc_A c_7 C_m^{cs1L}, \\ g_{23} = QSc_A c_7 C_m^{cs2R}, \\ g_{24} = QSc_A c_7 C_m^{cs2L}, \\ g_{25} = QSc_A c_7 C_m^{vcsR}, \\ g_{26} = QSc_A c_7 C_m^{vcsL}, \end{cases}$$

$$\begin{cases} g_{31} = QSb\left(c_4 C_l^{cs1R} + c_9 C_n^{cs1R}\right), \\ g_{32} = QSb\left(c_4 C_l^{cs1L} + c_9 C_n^{cs1L}\right), \\ g_{33} = QSb\left(c_4 C_l^{cs2R} + c_9 C_n^{cs2R}\right), \\ g_{34} = QSb\left(c_4 C_l^{cs2L} + c_9 C_n^{cs2L}\right), \\ g_{35} = QSb\left(c_4 C_l^{vcsR} + c_9 C_n^{vcsR}\right), \\ g_{36} = QSb\left(c_4 C_l^{vcsL} + c_9 C_n^{vcsL}\right). \end{cases}$$

REFERENCES

[1] T. A. Weisshaar, "Morphing aircraft systems: Historical perspectives and future challenges," *Journal of Aircraft*, vol. 50, pp. 337-353, 2013.

[2] R. M. Ajaj, C. S. Beaverstock, and M. I. Friswell, "Morphing aircraft: The need for a new design philosophy," *Aerospace Science & Technology*, vol. 49, pp. 154-166, 2016.

[3] S. Barbarino, O. Bilgen, R. M. Ajaj, M. I. Friswell, and D. J. Inman, "A review of morphing aircraft," *Journal of Intelligent Material Systems and Structures*, vol. 22, pp. 823-877, 2011.

[4] J. Bowman, B. Sanders, and T. Weisshaar, "Evaluating the impact of morphing technologies on aircraft performance," *Proc. of 43rd AIAA/ASME/ASCE/AHS/ASC Structures, Structural Dynamics, and Materials Conference*, p. 1631, 2002.

[5] P. Bourdin, A. Gatto, and M. Friswell, "Aircraft control via variable cant-angle winglets," *Journal of Aircraft*, vol. 45, pp. 414-423, 2008.

[6] R. Ajaj, M. Friswell, E. S. Flores, O. Little, and A. Isikveren, "Span morphing: A conceptual design study," *Proc. of 53rd AIAA/ASME/ASCE/AHS/ASC Structures, Structural Dynamics and Materials Conference 20th AIAA/ASME/AHS Adaptive Structures Conference 14th AIAA*, p. 1510, 2012.

[7] T. Yue, L. Wang, and J. Ai, "Flight performance characteristics of a tailless folding wing morphing aircraft," *Proc. of 51st AIAA Aerospace Sciences Meeting including the New Horizons Forum and Aerospace Exposition*, p. 623, 2013.

[8] R. M. Ajaj, M. I. Friswell, E. I. Saavedra Flores, A. Keane, A. T. Isikveren, G. Allegri, and S. Adhikari, "An integrated conceptual design study using span morphing technology," *Journal of Intelligent Material Systems and Structures*, vol. 25, pp. 989-1008, 2014.

[9] S. Joshi, Z. Tidwell, W. Crossley, and S. Ramakrishnan, "Comparison of morphing wing stategies based upon aircraft performance impacts," *Proc. of 45th AIAA/ASME/ASCE/AHS/ASC Structures, Structural Dynamics & Materials Conference*, p. 1722, 2004.

[10] N. Gandhi, J. Cooper, D. Ward, D. Howard, D. Neal, and B. Cannon, "A hardware demonstration of an integrated adaptive wing shape and flight control law for morphing aircraft," *Proc. of AIAA Guidance, Navigation, and Control Conference*, p. 5890, 2009.

[11] Z. Wu, J. Lu, J. Rajput, J. Shi, and W. Ma, "Adaptive neural control based on high order integral chained differentiator for morphing aircraft," *Mathematical Problems in Engineering*, vol. 2015, Article ID 787931, 2015.

[12] Z. Wu, J. Lu, J. Shi, Y. Liu, and Q. Zhou, "Robust adaptive neural control of morphing aircraft with prescribed performance," *Mathematical Problems in Engineering*, vol. 2017, Article ID 1401427, 2017.

[13] Z. Wu, J. Lu, Q. Zhou, and J. Shi, "Modified adaptive neural dynamic surface control for morphing aircraft with input and output constraints," *Nonlinear Dynamics*, vol. 87, pp. 2367-2383, 2017.

[14] Q. Wang, L. Gong, C. Dong, and K. Zhong, "Morphing aircraft control based on switched nonlinear systems and adaptive dynamic programming," *Aerospace Science and Technology*, vol. 93, 105325, 2019.

[15] B. Yan, Y. Li, P. Dai, and S. Liu, "Aerodynamic analysis, dynamic modeling, and control of a morphing aircraft," *Journal of Aerospace Engineering*, vol. 32, no. 5, 04019058, 2019.

[16] B. Yan, P. Dai, R. Liu, M. Xing, and S. Liu, "Adaptive super-twisting sliding mode control of variable sweep morphing aircraft," *Aerospace Science and Technology*, vol. 92, pp. 198-210, 2019.

[17] L. Tong and H. Ji, "Multi-body dynamic modelling and flight control for an asymmetric variable sweep morphing uav," *The Aeronautical Journal*, vol. 118, pp. 683-706, 2014.

[18] D. T. Grant, M. Abdulrahim, and R. Lind, "Flight dynamics of a morphing aircraft utilizing independent multiple-joint wing sweep," *International Journal of Micro Air Vehicles*, vol. 2, pp. 91-106, 2010.

[19] A. Chakravarthy, D. T. Grant, and R. Lind, "Time-varying dynamics of a micro air vehicle with variable-sweep morphing," *Journal of Guidance, Control, and Dynamics*, vol. 35, pp. 890-903, 2012.

[20] T. Yue, L. Wang, and J. Ai, "Longitudinal linear parameter varying modeling and simulation of morphing aircraft," *Journal of Aircraft*, vol. 50, pp. 1673-1681, 2013.

[21] T. Yue, L. Wang, and J. Ai, "Gain self-scheduled $h\infty$ control for morphing aircraft in the wing transition process based on an LPV model," *Chinese Journal of Aeronautics*, vol. 26, pp. 909-917, 2013.

[22] X. Jiao and J. Jiang, "Learning control law of mode switching for hypersonic morphing aircraft based on type-2 TSK fuzzy neural network," *International Journal of Machine Learning and Computing*, vol. 5, pp. 301-306, 2015.

[23] T. Yue, X. Zhang, L. Wang, and J. Ai, "Flight dynamic modeling and control for a telescopic wing morphing aircraft via asymmetric wing morphing," *Aerospace Science and Technology*, vol. 70, pp. 328-338, 2017.

[24] Z. Hui, Y. Zhang, and G. Chen, "Aerodynamic performance investigation on a morphing unmanned aerial vehicle with bio-inspired discrete wing structures," *Aerospace Science and Technology*, vol. 95, 105419, 2019.

[25] D. Xu, Z. Hui, Y. Liu, and G. Chen, "Morphing control of a new bionic morphing uav with deep reinforcement learning," *Aerospace Science and Technology*, vol. 92, pp. 232-243, 2019.

[26] M. Lungu, "Auto-landing of fixed wing unmanned aerial vehicles using the backstepping control," *ISA Transactions*, vol. 95, pp. 194-210, 2019.

[27] S. Zeghlache, A. Djerioui, L. Benyettou, T. Benslimane, H. Mekki, and A. Bouguerra, "Fault tolerant control for modified quadrotor via adaptive type-2 fuzzy backstepping subject to actuator faults," *ISA transactions*, vol. 95, pp. 330-345, 2019.

[28] M. Lungu, "Backstepping and dynamic inversion combined controller for auto-landing of fixed wing uavs," *Aerospace Science and Technology*, vol. 96, 105526, 2020.

[29] Y. Zhang, S. Wang, B. Chang, and W. Wu, "Adaptive constrained backstepping controller with prescribed performance methodology for carrier-based UAV," *Aerospace Science and Technology*, vol. 92, pp. 55-65, 2019.

[30] T. Lee and Y. Kim, "Nonlinear adaptive flight control using backstepping and neural networks controller," *Journal of Guidance, Control, and Dynamics*, vol. 24, pp. 675-682, 2001.

[31] C.-Y. Li, W.-X. Jing, and C.-S. Gao, "Adaptive backstepping-based flight control system using integral filters," *Aerospace Science and Technology*, vol. 13, pp. 105-113, 2009.

[32] A. Sharafian, V. Bagheri, and W. Zhang, "RBF neural network sliding mode consensus of multiagent systems with unknown dynamical model of leader-follower agents," *International Journal of Control, Automation, and Systems*, vol. 16, pp. 749-758, 2018.

[33] Y. Wang, L. Cao, S. Zhang, X. Hu, and F. Yu, "Command filtered adaptive fuzzy backstepping control method of uncertain non-linear systems," *IET Control Theory & Applications*, vol. 10, pp. 1134-1141, 2016.

[34] H. K. Khalil and J. W. Grizzle, *Nonlinear Systems*, Prentice Hall Upper Saddle River, NJ, 2002.

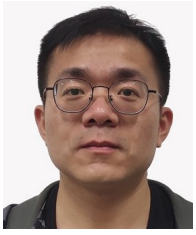

Fuxiang Qiao was born in 1991. He received his B.S. degree from Northwestern Polytechnical University. He is currently pursuing a Ph.D. degree in control theory and control engineering. His main research interests are flight control technology of morphing aircraft. He published 3 papers in relevant fields.

Jingping Shi is a Doctor of Engineering, postdoctoral, associate professor of Northwest Polytechnic University. His main research fields are flight control technology, over-drive system control allocation technology, parafoil control technology, optimization algorithm, etc. He presided over one project of the National Natural Fund, two projects of the Aviation Fund and 15 other projects. One award was awarded for outstanding teaching achievements. More than 16 academic papers have been published in important journals and international conferences.

Xiaobo Qu received his Doctor of Engineering from Northwestern Polytechnical University, where he holds a postdoctoral position and also an Assistant Researcher. He has published more than ten academic articles and applied for six patents in important journals and international conferences. His current research interests include flight control technology, over-drive systems control allocation technology, optimization of new concept UAV, intelligent control algorithm, aerodynamic coupling analysis, and the optimization of close formation of UAVs.

Yongxi Lyu was born in June 1990. He is an assistant researcher, Doctor of Engineering. His main research directions are high-angle-of-attack flight control technology, high-angle-of-attack aerodynamic modeling technology and multi-control plane control allocation technology. He has participated in a number of research projects such as the National Natural Resources Fund, and he also published nearly 10 papers and patents in academic conferences and journals.

Publisher's Note Springer Nature remains neutral with regard to jurisdictional claims in published maps and institutional affiliations.